

Dynamic analysis of a 3D driver–vehicle coupled vibration under pavement roughness excitation

Chaohe Wang, Markus Oeser & Pengfei Liu

To cite this article: Chaohe Wang, Markus Oeser & Pengfei Liu (2026) Dynamic analysis of a 3D driver–vehicle coupled vibration under pavement roughness excitation, International Journal of Pavement Engineering, 27:1, 2642963, DOI: [10.1080/10298436.2026.2642963](https://doi.org/10.1080/10298436.2026.2642963)

To link to this article: <https://doi.org/10.1080/10298436.2026.2642963>



© 2026 The Author(s). Published by Informa UK Limited, trading as Taylor & Francis Group.



Published online: 19 Mar 2026.



Submit your article to this journal [↗](#)



Article views: 71




View related articles [↗](#)



View Crossmark data [↗](#)

Dynamic analysis of a 3D driver–vehicle coupled vibration under pavement roughness excitation

Chaohe Wang^a, Markus Oeser^{a,b} and Pengfei Liu^a 

^aInstitute of Highway Engineering, RWTH Aachen University, Aachen, Germany; ^bFederal Highway Research Institute (BASt), Bergisch Gladbach, Germany

ABSTRACT

Vibrations directly affect occupants' perception, comfort and health during driving. However, comprehensive evaluations of vibration effects on the human body remain limited and there is less guidance for passenger cars driving from the driver's perspective. In this study, an 18-degree-of-freedom (DOF) 3D driver–vehicle coupled vibration model considering various parts of the driver and vehicle was established. Based on the index of comfort, motion sickness and vibration exposure risk to various organs, driving conditions for cars were proposed. The partial correlation analysis was used to explore the effects of pavement roughness, driving speed and riding time. The results showed that the driving comfort index increased with the deterioration of roughness and the increase of driving speed. The motion sickness index (MSI) increased linearly with the deterioration of unevenness and the increase in riding time, but showed no obvious relationship with speed under the same traveling time. Pavement roughness had the greatest influence on both comfort and motion sickness. Vibrations most strongly affected the stomach, lumbar spine, liver and head. It was recommended to control pavement roughness to power spectral density (PSD)-based Level A and to pay particular attention to operating conditions above about 100 km/h.

ARTICLE HISTORY

Received 26 July 2024
Accepted 3 March 2026

KEYWORDS

3D driver–vehicle coupled vibration model; driving comfort; motion sickness; vibration exposure risk to organs; transportation engineering

1. Introduction

Drivers experience low-frequency vibrations that are associated with discomfort, fatigue, drowsiness and other adverse health effects while driving (Voicu et al., 2023). Occupant–vehicle coupling modelling is an important method to study driving comfort, motion sickness and vibration exposure risk to human organs during the travelling process. Wei et al. (2020a, 2020b) (Wu et al., 2021) proposed a ‘human–vehicle shared control’ dynamics model that considered the driver's neuromuscular characteristics, combining vehicle state feedback and driver state. The results provide a theoretical basis for the allocation of control strategies between humans and vehicles in the shared control process of L3-level autonomous vehicles. Desai et al. (2021) established a 12-DOF seated human–nonlinear seat cushion–full vehicle model and the sensitivity of a multi-compression damper with an inclined damper–seat suspension system was investigated by using random road surfaces and sudden bumps for pavement excitation. The results showed that the inclination angle of the damper was the parameter with the highest sensitivity. Luo (2021) utilised ADAMS/Car software to develop a multibody dynamics model for a human–vehicle system and investigated the effect of human–vehicle dynamics coupling on the roll stability of a miniature electric vehicle. The results showed that the roll stability of the car decreased considering the human. Song et al. (2023) developed a fully coupled human–vehicle model using CarSim software and MATLAB/Simulink and computed ride comfort using the generalised polynomial method. The results showed that the nonlinearity of the human model was important for the stochastic estimation of ride comfort. Prior studies on the dynamic models of the human body and vehicles have generally used them to assess ride comfort and its influence on vehicle behaviour. For occupants, assessing ride comfort alone is inadequate. The entire process, from comfort perception to vibration exposure risk assessment, should be comprehensively

CONTACT Pengfei Liu  liu@isac.rwth-aachen.de

© 2026 The Author(s). Published by Informa UK Limited, trading as Taylor & Francis Group. This is an Open Access article distributed under the terms of the Creative Commons Attribution License (<http://creativecommons.org/licenses/by/4.0/>), which permits unrestricted use, distribution, and reproduction in any medium, provided the original work is properly cited. The terms on which this article has been published allow the posting of the Accepted Manuscript in a repository by the author(s) or with their consent.

analysed during vehicle travel. Based on these results, recommendations and guidance should be provided to optimise vehicle operation.

For motion sickness, Chang et al. (2020) analysed the effects of physical driving experience on the passenger's body and motion sickness in a virtual vehicle and showed that physical driving experience was associated with postural activity patterns before motion sickness. Li et al. (2021) conducted a rear-seat VR study on an urban freeway. The results showed that a range of head motion of $\pm 50^\circ$ and a speed of 1.95 m/s was the best trade-off between motion sickness and engagement. Asua et al. (2022) experimentally investigated the effects of driving style, vehicle and road characteristics on comfort and motion sickness. They found that comfort was highly correlated with road type and that longitudinal and lateral accelerations had a significantly greater impact on comfort than vertical acceleration. Wada et al. (2024) investigated the effects of passenger body movement on post-rotation illusions and motion sickness during a visual task during and after vehicle rotation. The results suggested that illusory motion could be used as an indicator of impending motion sickness and that body movement during and after continuous rotation had a significant effect on illusory intensity. Based on an analysis of existing literature, motion sickness research was mostly conducted using real vehicle tests or virtual driving simulation platforms. From a theoretical perspective, there were few studies on the occurrence and development of motion sickness through whole-body vibration of passengers and drivers. It is of great significance to reduce the occurrence of motion sickness and provide suggestions for the driving speed and pavement roughness status.

Long-term exposure to low-frequency vibrations generated by vehicle driving can harm human health (Fan et al., 2018). Regarding the risk caused by vibration to the human body, Fan et al. (2018, 2019) and Fan et al. (2021) used the resonance method to predict the natural frequency value of the human lumbar spine, thereby optimising the vibration generated in the working and living environment and avoiding resonance. Voicu et al. (2023) used power spectral density and diagonal line quantification methods to evaluate the whole-body vibration and hand-arm vibration exposure of drivers in armoured personnel carriers and cargo-destined vehicles. To protect the driver from fatigue and injury, a resilient and damped connection between the vehicle and the driver's seat is necessary. The vibration experienced by occupants during driving is a whole-body vibration. The effect of vibration on human organs in previous research was studied in terms of the lumbar spine, arms and head, but few other parts, including internal organs, reproductive system, etc., have been analysed. Therefore, assessing the vibration exposure risk of various organs in the human body based on the whole-body vibration response is a useful supplement to existing research.

In summary, comprehensive research on the response of the driver during vehicle travel is still insufficient. Therefore, this paper established an 18-DOF 3D driver-vehicle coupled vibration dynamics model based on the 3D contact characteristics of the tyre and road surface. The effects of different pavement roughness excitations, different travelling speeds and different driving times on the comfort, motion sickness and vibration exposure risks of human organs were analysed and relevant suggestions were put forward. The flowchart is shown in Figure 1. This study provides a theoretical basis for decision-making and control of the vehicle from the driver's perspective.

2. Theoretical derivation and model construction

2.1. 3D driver-vehicle coupling vibration modelling

To overcome the limitations of existing occupant-vehicle coupled models, this study proposed a novel 18-DOF dynamic model that integrated the vibration of a full passenger car with a biomechanically representative seated human body model. Unlike previous studies that simplified the human body into a limited number of mass segments or overlooked its dynamic interaction with the vehicle, the proposed model incorporated multiple body components and their coupling with vehicle vibrations, enabling a more accurate evaluation of the vibration response. Furthermore, a 3D tyre-pavement contact model (Wang et al., 2023), previously developed by the authors, was embedded to realistically capture the interaction between the road surface and tyres. This integration allows for the simultaneous evaluation of driving comfort, motion sickness and organ-level vibration exposure, thereby providing a comprehensive framework for studying driver vibration and vehicle dynamics under 3D pavement roughness excitations.

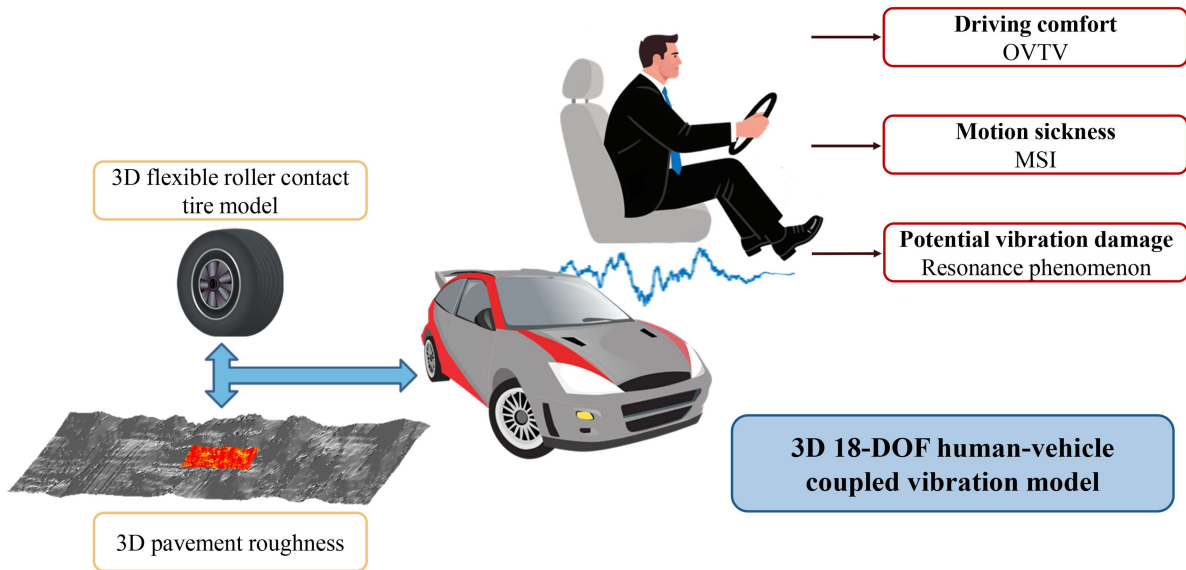


Figure 1. Flowchart of the research method.

It should be noted that the pavement roughness profiles used in this study were classified based on their PSD characteristics, which are suitable as input for dynamic vehicle-human vibration simulations. Although the International Roughness Index (IRI) is widely used in pavement engineering, there is currently no standardised or validated mapping between PSD-based roughness levels and IRI values. Therefore, PSD-based A-C levels were employed in this study and the present analysis focuses on their influence on human vibration responses. Establishing a quantitative relationship between PSD-based profiles and IRI, as well as identifying roughness spectral features that most significantly affect motion sickness, remains an important topic for future work to enhance the practical applicability of the model.

This model had the following six assumptions: (i) only the vertical vibration of each part of the body was considered and the effect of the seat back was ignored (Qassem et al., 1994; Taskin et al., 2018); (ii) a rigid connection was used between the seat and the vehicle; (iii) the vehicle was simplified as a ‘mass-stiffness-damping’ dynamical system; (iv) the suspension system was simulated by a linear spring and a linear damper in parallel and the stiffness and damping were constants; (v) the road was a rigid cement concrete pavement without considering the modulus of each structural layer and the vibration of the road structure and (vi) the proposed model was developed under linear assumptions and continuous contact conditions between the tyre and pavement, as well as between the driver and the seat. An 18-DOF 3D driver-vehicle coupled vibration model was established, as shown in Figure 2.

The mass of the legs and feet was not included in the human body model because these body parts had a negligible response to seated human biodynamics (Taskin et al., 2018).

In Figure 2, where $m_{h/n/la/ua/tor/tho-spi/tho/d/l/a/p}$ represents head mass, neck mass, lower arm mass, upper arm mass, torso mass, thoracic spine mass, thorax mass, diaphragm mass, lumbar spine mass, abdomen mass and pelvis mass; $c_{h/n/la/ua/tor/tho-spi/tho/d/l/a/p}$ represents head damping, neck damping, lower arm damping, upper arm damping, torso damping, thoracic spine damping, thorax damping, diaphragm damping, lumbar spine damping, abdomen damping and pelvis damping; $k_{h/n/la/ua/tor/tho-spi/tho/d/l/a/p}$ represents head stiffness, neck stiffness, lower arm stiffness, upper arm stiffness, torso stiffness, thoracic spine stiffness, thorax stiffness, diaphragm stiffness, lumbar spine stiffness, abdomen stiffness and pelvis stiffness; $m_{r/t(f/r)}$ represents sprung and seat mass and four unsprung masses; $c_{r(t/r)/t(f/r)}$ represents suspension damping and tyre damping; $k_{r(t/r)/t(f/r)}$ represents suspension stiffness and tyre stiffness; $z_{r/t(f/r)}$ represents the vertical displacement of the sprung mass and unsprung masses; $z_q(f/r)$ are left and right pavement roughness elevations; J and I represent the pitching inertia and roll inertia of the vehicle; α and β are pitch motion inclination angle and roll motion inclination angle; a and b represent the distances

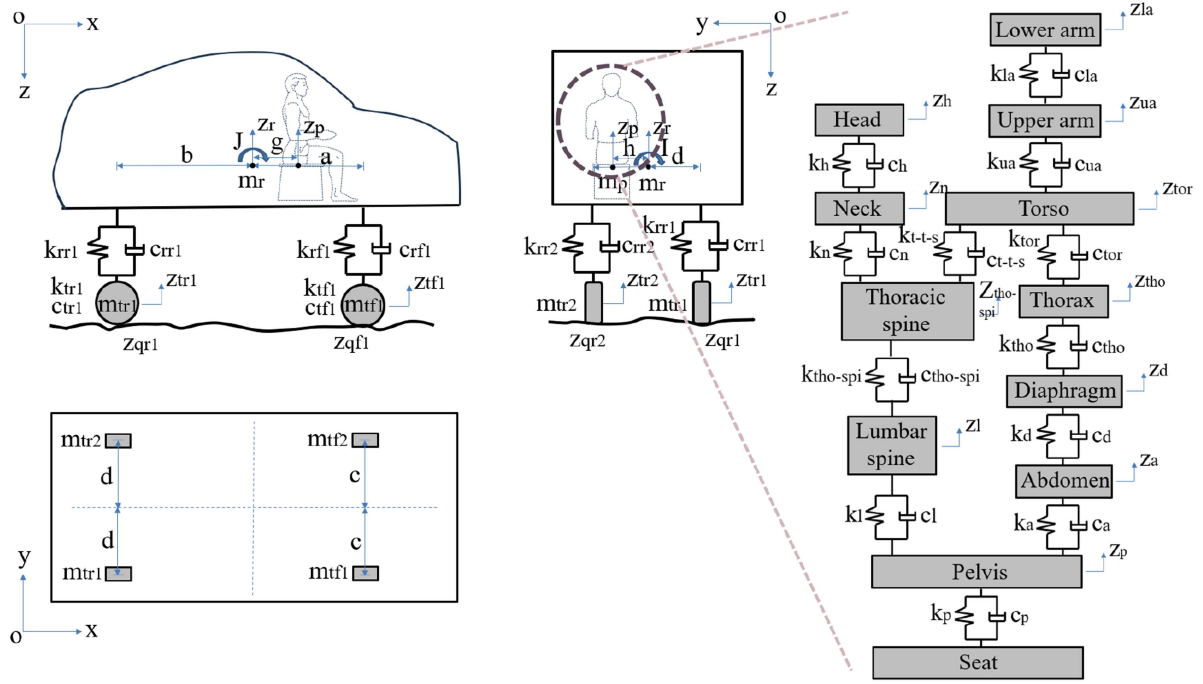


Figure 2. The 3D dynamic model of 18-DOF driver-vehicle coupled vibration, including car (left) and human (right).

from the front and rear axles to the centre of mass; c and d are half the centre distance of the front axle and rear axle; g and h represent the longitudinal and lateral distances between the seat centre of mass and the vehicle centre of mass, respectively.

Based on the D'Alembert principle, the dynamic equilibrium equations are shown in Equations (1)–(18).

The vertical vibration equation of the head is,

$$m_h \ddot{z}_h + c_h (\dot{z}_h - \dot{z}_n) + k_h (z_h - z_n) = 0. \quad (1)$$

The vertical vibration equation of the neck is,

$$m_n \ddot{z}_n + c_n (\dot{z}_n - \dot{z}_{tho-spi}) + k_n (z_n - z_{tho-spi}) - c_h (\dot{z}_h - \dot{z}_n) - k_h (z_h - z_n) = 0 \quad (2)$$

The vertical vibration equation of the lower arm is,

$$m_{la} \ddot{z}_{la} + c_{la} (\dot{z}_{la} - \dot{z}_{ua}) + k_{la} (z_{la} - z_{ua}) = 0. \quad (3)$$

The vertical vibration equation of the upper arm is,

$$m_{ua} \ddot{z}_{ua} + c_{ua} (\dot{z}_{ua} - \dot{z}_{tor}) + k_{ua} (z_{ua} - z_{tor}) - c_{la} (\dot{z}_{la} - \dot{z}_{ua}) - k_{la} (z_{la} - z_{ua}) = 0 \quad (4)$$

The vertical vibration equation of the torso is,

$$m_{tor} \ddot{z}_{tor} + c_{tor} (\dot{z}_{tor} - \dot{z}_{tho}) + k_{tor} (z_{tor} - z_{tho}) + c_{t-t-s} (\dot{z}_{tor} - \dot{z}_{tho-spi}) + k_{t-t-s} (z_{tor} - z_{tho-spi}) - c_{ua} (\dot{z}_{ua} - \dot{z}_{tor}) - k_{ua} (z_{ua} - z_{tor}) = 0 \quad (5)$$

The vertical vibration equation of the thoracic spine is,

$$\begin{aligned} & m_{tho-spi} \ddot{z}_{tho-spi} + c_{tho-spi} (\dot{z}_{tho-spi} - \dot{z}_l) + k_{tho-spi} (z_{tho-spi} - z_l) \\ & - c_{t-t-s} (\dot{z}_{tor} - \dot{z}_{tho-spi}) - k_{t-t-s} (z_{tor} - z_{tho-spi}) \\ & - c_n (\dot{z}_n - \dot{z}_{tho-spi}) - k_n (z_n - z_{tho-spi}) = 0 \end{aligned} \quad (6)$$

The vertical vibration equation of the thorax is,

$$\begin{aligned} & m_{tho} \ddot{z}_{tho} + c_{tho} (\dot{z}_{tho} - \dot{z}_d) + k_{tho} (z_{tho} - z_d) \\ & - c_{tor} (\dot{z}_{tor} - \dot{z}_{tho}) - k_{tor} (z_{tor} - z_{tho}) = 0 \end{aligned} \quad (7)$$

The vertical vibration equation of the diaphragm is,

$$\begin{aligned} & m_d \ddot{z}_d + c_d (\dot{z}_d - \dot{z}_a) + k_d (z_d - z_a) \\ & - c_{tho} (\dot{z}_{tho} - \dot{z}_d) - k_{tho} (z_{tho} - z_d) = 0 \end{aligned} \quad (8)$$

The vertical vibration equation of the lumbar spine is,

$$\begin{aligned} & m_l \ddot{z}_l + c_l (\dot{z}_l - \dot{z}_p) + k_l (z_l - z_p) \\ & - c_{tho-spi} (\dot{z}_{tho-spi} - \dot{z}_l) - k_{tho-spi} (z_{tho-spi} - z_l) = 0 \end{aligned} \quad (9)$$

The vertical vibration equation of the abdomen is,

$$m_a \ddot{z}_a + c_a (\dot{z}_a - \dot{z}_p) + k_a (z_a - z_p) - c_d (\dot{z}_d - \dot{z}_a) - k_d (z_d - z_a) = 0. \quad (10)$$

The vertical vibration equation of the pelvis is,

$$\begin{aligned} & m_p \ddot{z}_p + c_p (\dot{z}_p - (\dot{z}_r + g\dot{\alpha} - h\dot{\beta})) + k_p (z_p - (z_r + g\alpha - h\beta)) \\ & - c_a (\dot{z}_a - \dot{z}_p) - k_a (z_a - z_p) - c_l (\dot{z}_l - \dot{z}_p) - k_l (z_l - z_p) = 0 \end{aligned} \quad (11)$$

The vertical vibration equation of sprung mass is,

$$\begin{aligned} & m_r \ddot{z}_r - c_p (\dot{z}_p - (\dot{z}_r + g\dot{\alpha} - h\dot{\beta})) - k_p (z_p - (z_r + g\alpha - h\beta)) \\ & + c_{rf1} (\dot{z}_r + a\dot{\alpha} + c\dot{\beta} - \dot{z}_{tf1}) + k_{rf1} (z_r + a\alpha + c\beta - z_{tf1}) \\ & + c_{rf2} (\dot{z}_r + a\dot{\alpha} - c\dot{\beta} - \dot{z}_{tf2}) + k_{rf2} (z_r + a\alpha - c\beta - z_{tf2}) \\ & + c_{rr1} (\dot{z}_r - b\dot{\alpha} + d\dot{\beta} - \dot{z}_{tr1}) + k_{rr1} (z_r - b\alpha + d\beta - z_{tr1}) \\ & + c_{rr2} (\dot{z}_r - b\dot{\alpha} - d\dot{\beta} - \dot{z}_{tr2}) + k_{rr2} (z_r - b\alpha - d\beta - z_{tr2}) = 0 \end{aligned} \quad (12)$$

The pitching motion equation of sprung mass is,

$$\begin{aligned} & J\ddot{\alpha} + c_p \cdot g (\dot{z}_r + g\dot{\alpha} - h\dot{\beta} - \dot{z}_p) + k_p \cdot g (z_r + g\alpha - h\beta - z_p) \\ & + c_{rf1} \cdot a (\dot{z}_r + a\dot{\alpha} + c\dot{\beta} - \dot{z}_{tf1}) + k_{rf1} \cdot a (z_r + a\alpha + c\beta - z_{tf1}) \\ & + c_{rf2} \cdot a (\dot{z}_r + a\dot{\alpha} - c\dot{\beta} - \dot{z}_{tf2}) + k_{rf2} \cdot a (z_r + a\alpha - c\beta - z_{tf2}) \\ & - c_{rr1} \cdot b (\dot{z}_r - b\dot{\alpha} + d\dot{\beta} - \dot{z}_{tr1}) - k_{rr1} \cdot b (z_r - b\alpha + d\beta - z_{tr1}) \\ & - c_{rr2} \cdot b (\dot{z}_r - b\dot{\alpha} - d\dot{\beta} - \dot{z}_{tr2}) - k_{rr2} \cdot b (z_r - b\alpha - d\beta - z_{tr2}) = 0 \end{aligned} \quad (13)$$

The roll motion equation of sprung mass is,

$$\begin{aligned} & I\ddot{\beta} - c_p \cdot h (\dot{z}_r + g\dot{\alpha} - h\dot{\beta} - \dot{z}_p) - k_p \cdot h (z_r + g\alpha - h\beta - z_p) \\ & + c_{rf1} \cdot c (\dot{z}_r + a\dot{\alpha} + c\dot{\beta} - \dot{z}_{tf1}) + k_{rf1} \cdot c (z_r + a\alpha + c\beta - z_{tf1}) \\ & - c_{rf2} \cdot c (\dot{z}_r + a\dot{\alpha} - c\dot{\beta} - \dot{z}_{tf2}) - k_{rf2} \cdot c (z_r + a\alpha - c\beta - z_{tf2}) \\ & + c_{rr1} \cdot d (\dot{z}_r - b\dot{\alpha} + d\dot{\beta} - \dot{z}_{tr1}) + k_{rr1} \cdot d (z_r - b\alpha + d\beta - z_{tr1}) \\ & - c_{rr2} \cdot d (\dot{z}_r - b\dot{\alpha} - d\dot{\beta} - \dot{z}_{tr2}) - k_{rr2} \cdot d (z_r - b\alpha - d\beta - z_{tr2}) = 0 \end{aligned} \quad (14)$$

The vertical vibration equation of the right front unsprung mass is,

$$\begin{aligned} m_{tf1}\ddot{z}_{tf1} - c_{rf1}(\dot{z}_r + a\dot{\alpha} + c\dot{\beta} - \dot{z}_{tf1}) - k_{rf1}(z_r + a\alpha + c\beta - z_{tf1}) \\ + c_{tf1}\dot{z}_{tf1} - F_{f12} + k_{tf1}r_0 + k_{tf1}z_{tf1} - F_{f11} = 0 \end{aligned} \quad (15)$$

The vertical vibration equation of the left front unsprung mass is,

$$\begin{aligned} m_{tf2}\ddot{z}_{tf2} - c_{rf2}(\dot{z}_r + a\dot{\alpha} - c\dot{\beta} - \dot{z}_{tf2}) - k_{rf2}(z_r + a\alpha - c\beta - z_{tf2}) \\ + c_{tf2}\dot{z}_{tf2} - F_{f22} + k_{tf2}r_0 + k_{tf2}z_{tf2} - F_{f21} = 0 \end{aligned} \quad (16)$$

The vertical vibration equation of the right rear unsprung mass is,

$$\begin{aligned} m_{tr1}\ddot{z}_{tr1} - c_{rr1}(\dot{z}_r - b\dot{\alpha} + d\dot{\beta} - \dot{z}_{tr1}) - k_{rr1}(z_r - b\alpha + d\beta - z_{tr1}) \\ + c_{tr1}\dot{z}_{tr1} - F_{r12} + k_{tr1}r_0 + k_{tr1}z_{tr1} - F_{r11} = 0 \end{aligned} \quad (17)$$

The vertical vibration equation of the left rear unsprung mass is,

$$\begin{aligned} m_{tr2}\ddot{z}_{tr2} - c_{rr2}(\dot{z}_r - b\dot{\alpha} - d\dot{\beta} - \dot{z}_{tr2}) - k_{rr2}(z_r - b\alpha - d\beta - z_{tr2}) \\ + c_{tr2}\dot{z}_{tr2} - F_{r22} + k_{tr2}r_0 + k_{tr2}z_{tr2} - F_{r21} = 0 \end{aligned} \quad (18)$$

A 3D flexible roller contact tyre model (Wang et al., 2023) was chosen for the tyre–pavement contact, where $F_{f(r)i1}$ and $F_{f(r)i2}$ are shown in Equations (19) and (20).

$$F_{f(r)i1} = \frac{k_{f(r)i}}{2m \cdot 2n} \int_{-m}^m \int_{-n}^n (q + \sqrt{r_0^2 - x_m^2}) dx dy, \quad (19)$$

$$F_{f(r)i2} = \frac{c_{f(r)i}}{2m \cdot 2n} \int_{-m}^m \int_{-n}^n \left(\frac{\partial q}{\partial t} + \frac{\partial \sqrt{r_0^2 - x_m^2}}{\partial t} \right) dx dy. \quad (20)$$

Combining Equations (1)–(18), the vehicle vibration differential equation was obtained as shown in Equation (21).

$$M\ddot{Z} + C\dot{Z} + KZ = F. \quad (21)$$

The central difference method (Ji & Xing, 2020; Wang et al., 2023) was used to solve the equation and passenger and vehicle parameters were based on existing studies (Taskin et al., 2018; Wang et al., 2023).

2.2. Driving comfort model and evaluation index

2.2.1. Selection of evaluation indexes for sitting human comfort

Based on the international standard ISO 2631-1 (1997), OVTV (Overall Vibration Total Value) (Zhu et al., 2023) was chosen as the evaluation index for driving comfort. There are five steps to calculate seated human comfort as follows (Zhu et al., 2023).

1. Calculate the acceleration of different parts of the driver in different directions: the position and direction of acceleration for a seated human body were illustrated in ISO 2631-1 (1997). It has been shown that yaw vibration has little effect on comfort, so the effect r_z was not considered (Zhu et al., 2023). Because the human vibration model in this study considered only vertical vibration, the rotational vibration and feet vibration in the comfort evaluation index were calculated based on the pitch and roll motion of the vehicle. Based on existing literature and the author's previous research (Wang et al., 2023; Zhu et al., 2023), the human body vibration responses are shown in Equations (22)–(28).

$$a_{xb} = a_{xs} = a_{xf} = \dot{\alpha}^2 g, \quad (22)$$

$$a_{yb} = a_{ys} = a_{yf} = \dot{\beta}^2 h, \quad (23)$$

$$a_{zb} = a_{tho-spi}, \quad (24)$$

$$a_{zs} = a_p, \quad (25)$$

$$a_{zf} = a_r, \quad (26)$$

$$a_{rx} = \ddot{\beta}h + \frac{1}{2}\ddot{\beta}h_s, \quad (27)$$

$$a_{ry} = \ddot{\alpha}g. \quad (28)$$

where a_{xb} , a_{yb} and a_{zb} represent axial vibration acceleration of the human back in three directions; a_{xs} , a_{ys} and a_{zs} represent axial vibration acceleration of the human hip in three directions; a_{xf} , a_{yf} and a_{zf} represent axial vibration acceleration of the human feet in three directions; a_{rx} represents roll vibration acceleration; a_{ry} represents pitch vibration acceleration of the human; $a_{tho-spi}$ represents vertical acceleration of the thoracic spine mass; a_p represents vertical acceleration of the pelvis mass; a_r represents vertical acceleration of the sprung and seat mass and h_s represents the vertical distance between the centre of mass of the vehicle and the seat.

2. Calculate the frequency-weighted acceleration time history $a_{wx(y/z/r)b(s/f/x/y)}(t)$: Since the human body has a different degree of sensitivity to the direction and frequency of vibration, the frequency-weighted function was used to filter the acceleration time history curve in each axial direction (ISO, 1997).

Frequency-weighted acceleration time history curves were calculated based on the fast Fourier convolution method (Zhu et al., 2023).

3. Calculate the quadratic root-mean-square (RMS) value of the frequency-weighted acceleration, as shown in Equation (29).

$$RMS_{x(y/z/r)b(s/f/x/y)} = \left[\frac{1}{T} \int_0^T a_{wx(y/z/r)b(s/f/x/y)}^2(t) dt \right]^{\frac{1}{2}}, \quad (29)$$

where T is the total duration of vibration.

4. Calculation of the OVTV: The OVTV is calculated as shown in Equation (30).

$$OVTV = \left[\sum (M_{x(y/z/r)b(s/f/x/y)} RMS_{x(y/z/r)b(s/f/x/y)})^2 \right]^{\frac{1}{2}}, \quad (30)$$

where $M_{x(y/z/r)b(s/f/x/y)}$ represents the axial weighting coefficients, which are adopted directly from ISO 2631-1 (1997) and vary according to body position and axis of measurement.

The OVTV calculation method makes it possible to calculate and evaluate comfort during driving.

2.2.2. Determination of comfort thresholds

The international standard ISO 2631-1 defines the correspondence between human vibration and different comfort levels, but does not give clear boundaries. Therefore, in this study, the membership function method (Wang & Zhang, 2014; Wang et al., 2023; Zhang et al., 2018; Li & Wang, 2020) was used to determine the clear boundaries of the different comfort levels of the occupant, as shown in Table 1.

From Table 1, OVTV was taken as 0.315 m/s^2 , which was the boundary between comfort and discomfort. During the travelling of passenger cars, the OVTV should be less than 0.315 m/s^2 .

Table 1. Limiting the values of driving comfort.

Classification of comfort level	OVTV (m/s ²)
Comfortable	Less than 0.315
A little uncomfortable	0.315–0.580
Relatively uncomfortable	0.580–0.920
Uncomfortable	0.920–1.460
Very uncomfortable	1.460–2.250
Extremely uncomfortable	Greater than 2.25

2.3. Motion sickness model and evaluation index

Based on the ISO 2631-1 standard, the MSI was selected as the evaluation index of motion sickness. The MSI is expressed as a percentage, indicating the proportion of vomiting in the crowd. The MSI is calculated in the following steps:

- (1) Calculate the vibration response of the driver in different parts and directions, which is the same as step 1 in the comfort evaluation.
- (2) Calculate the frequency-weighted acceleration timescale $a'_{wz(r)b(s/f/x/y)}(t)$: the frequency-weighted function for motion sickness is W_f . The acceleration responses a_{zb} , a_{zs} , a_{zf} , a_{rx} and a_{ry} in the specifications that are directly related to motion sickness were selected for frequency modulation. The frequency-weighted accelerations a'_{wzb} , a'_{wzs} , a'_{wzf} , a'_{wrx} and a'_{wry} were obtained by the fast Fourier convolution method (Zhu et al., 2023).
- (3) Calculate the Motion Sickness Dose Value (MSDV) as shown in Equation (31).

$$\text{MSDV}_{z(r)b(s/f/x/y)} = \left[\int_0^T a'^2_{wz(r)b(s/f/x/y)}(t) dt \right]^{\frac{1}{2}}. \quad (31)$$

- (4) The total MSDV was calculated as shown in Equation (32). The axis weighting coefficients were all taken as 1.

$$\text{MSDV} = \left[\sum (\text{MSDV}_{z(r)b(s/f/x/y)})^2 \right]^{\frac{1}{2}}. \quad (32)$$

The motion sickness indicator (MSI) was calculated as shown in Equation (33). The unit of MSI is the percentage.

$$\text{MSI}(\%) = K_m \text{MSDV}, \quad (33)$$

where $K_m = 1/3$.

The limit for human motion sickness was $\text{MSI} = 30\%$ according to the International Standard ISO 2631-1, which means that 30% of people feel dizzy in a crowd.

The $\text{MSI} = 1\%$ was also used as a marker for the beginning of motion sickness and $\text{MSI} = 30\%$ was used as the maximum limit value of motion sickness (ISO, 1997).

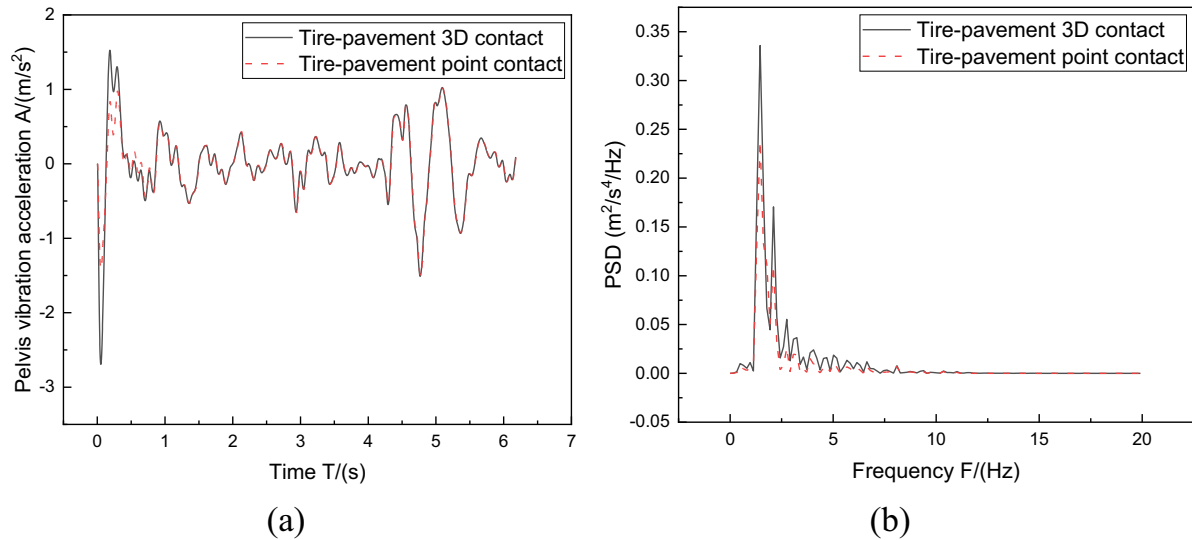
2.4. Evaluation of vibration exposure risk to driver organs

The driver will be affected by vibration during the driving process. The evaluation of vibration exposure risks to human organs is based on resonance theory. If the vibration frequency is the same or similar to the natural vibration frequency of human organs, it will produce a resonance phenomenon and increase the risk of vibration exposure. According to the time domain curves of the different organs' vibration, the PSD was calculated using the direct method to obtain the vibration response in the frequency domain. Then, by referencing the reported natural frequency ranges of specific organs, the PSD peaks within these ranges were extracted and compared across different pavement roughnesses and vehicle speed conditions. Larger PSD magnitudes within an organ's resonance range are interpreted as a higher potential for resonance excitation, which may imply increased vibration exposure risk.

The natural vibration frequencies (Fan et al., 2019, 2021; Więckowski, 2012) of different organs of the human body are shown in Table 2.

Table 2. Natural vibration frequencies of different organs in the human body.

Organs	Natural frequency [Hz]	Organs	Natural frequency [Hz]
Head	4~5	Trachea and bronchi	12~16
Neck	20~30	Lumbar spine	3~5
Lower arm	16~30	Stomach	2~3
Upper arm	4~6	Liver	3~4
Torso	4~5	Kidneys	6~8
Thoracic spine	10~12	Urinary bladder	10~18
Heart and lung	4~6	Pelvis	5~9

**Figure 3.** Comparison of pelvis vibration acceleration: (a) time domain and (b) frequency domain.

As can be seen from Table 2, the natural vibration frequency of each organ in the human body is low. The vibration generated during vehicle driving was also a low-frequency vibration (Hassan & Kerry, 2002). Therefore, the vibration frequencies transmitted to the driver's organs are more likely to coincide with their natural frequencies, thereby increasing the risk of vibration exposure.

3. Results and discussion

3.1. Model verification

To verify the accuracy of the 3D driver-vehicle coupled vibration model in Section 2.1, a traditional 18-DOF tyre-pavement point contact model was used.

The condition was set as two vehicle models travelling at 80 km/h on a Class A roughness pavement and the obtained pelvis vibration responses are shown in Figure 3.

As shown in Figure 3, the time-domain acceleration signals obtained from the two models exhibited a high degree of similarity in the waveform. The RMS value of the pelvis vibration acceleration calculated by the 3D model was $0.5 m/s^2$, while the RMS value calculated by the traditional point contact model was $0.413 m/s^2$. The tyre-pavement point contact model was 17.4% lower than the 3D contact model. In the frequency domain, both models exhibited dominant peaks at the same frequencies, indicating consistent system resonance characteristics. However, the PSD values of the point contact model were consistently lower than those of the 3D contact model across the frequency range. This discrepancy can be attributed to the differences in contact modelling fidelity. The 3D contact model captures the distributed nature of the tyre-road interaction, allowing for a more accurate representation of force transmission and dynamic excitation, which leads to a stronger vibration response and higher energy content at each frequency. In contrast, the point contact model oversimplifies the contact interface, effectively attenuating the excitation input and underestimating the energy transfer, thereby producing lower RMS and PSD values. These

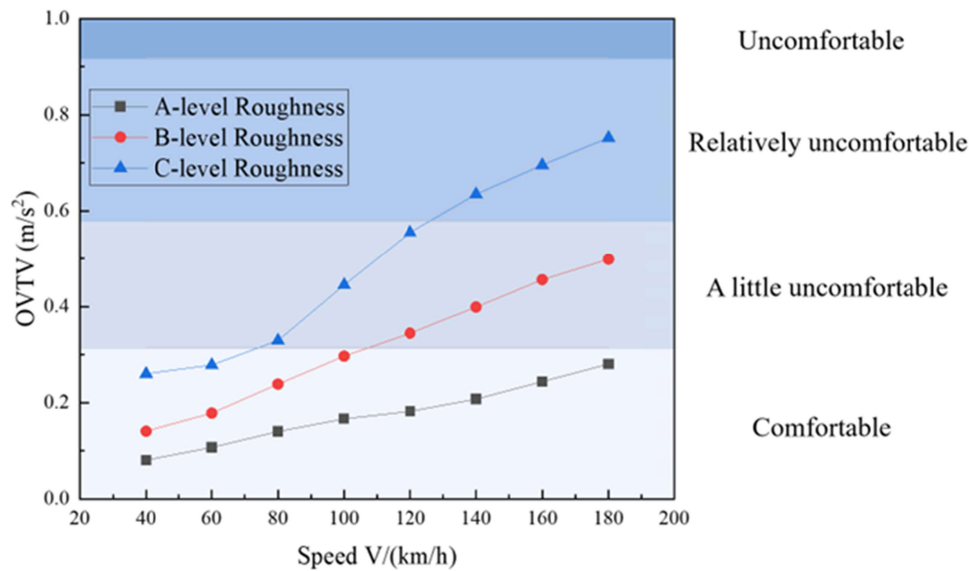


Figure 4. Driving comfort evaluation.

Table 3. Driving comfort speed decision for vehicle driving.

Classification of comfort level	Pavement roughness		
	A-level	B-level	C-level
Comfortable	–	107 km/h	76 km/h
A little uncomfortable	–	–	126 km/h
Relatively uncomfortable	–	–	–
Uncomfortable	–	–	–

results highlight the importance of accurate tyre-road contact modelling in simulating human-vehicle-road coupled dynamics.

3.2. Driving comfort analysis

Based on the comfort indicator OVTV, whose calculation equation is given in Equation (30) and the thresholds presented in Table 1, the results of the driving comfort evaluation are shown in Figure 4.

Based on Figure 4, it could be seen that when a car is driving on roads with different roughness levels, different comfort levels correspond to different driving speeds, as shown in Table 3.

As shown in Figure 4 and Table 3, when the passenger car travelled at a speed of less than 180 km/h on an A-level rough road, it would not adversely affect the comfort; When the car was driven on a B-level roughness pavement, with the increase in speed, the subjective feeling of the driver will change from ‘comfortable’ to ‘a little uncomfortable’ and the critical speed was 107 km/h. For class C unevenness pavement, when the speed was lower than 76 km/h, the driver would feel ‘comfortable’. When the speed was controlled between 76 km/h and 126 km/h, the human body would feel ‘a little uncomfortable’ and when the driving speed was greater than 126 km/h, the driver would feel ‘relatively uncomfortable’.

The comfort evaluation based on ISO 2631-1 adopts the RMS approach, which normalises acceleration over the total exposure duration. Although time is part of the calculation, the final comfort index represents an average level and is therefore relatively less sensitive to exposure time.

To analyse the degree of influence of pavement roughness and driving speed on comfort, a partial correlation analysis was conducted. The results showed that the partial correlation coefficient between driving comfort and pavement roughness was 0.8979 and the partial correlation coefficient between driving comfort and travel speed was 0.8918. Therefore, pavement roughness has a greater effect on comfort than speed. A reasonable driving speed should be determined based on the state of road unevenness. It is recommended to control the pavement roughness to Class A.

3.3. Motion sickness analysis

According to the MSI equation (calculated using Equation (33)), motion sickness is related to the pavement roughness, driving speed and travel time.

3.3.1. Impact of pavement roughness

The vehicle driving distance was 40,000 m, the results of the MSI when the car was driving at different speeds on different road rough surfaces were obtained, as shown in Figure 5.

As can be seen from Figure 5, when the road length and speed were constant, the worse the pavement roughness was, the more likely it was to cause motion sickness in humans. The lower the speed, the more obvious the motion sickness caused by pavement roughness. When the driving speed was 40 km/h, the road surface unevenness deteriorated from Grade A to Grade B and then to Grade C and the MSI increased from 1.07% to 1.82% and then to 3.06%, which was an increase of 70% and 185.98%, respectively. Under the same roughness, the MSI gradually decreased with increasing speed. From 40 km/h to 180 km/h, the worse the roughness grade, the greater the rate of decrease of MSI and the change rates of the MSI corresponding to levels A, B and C roughness were 48.98%, 49.23% and 56.46%, respectively. Therefore, to reduce the occurrence of motion sickness, the road surface should be kept smooth while reducing travel time and appropriately increasing the driving speed.

3.3.2. Impact of driving speed

The driving time was 20 min and the results of MSI when the car was driven at different speeds on different pavement roughnesses were obtained, as shown in Figure 6.

As shown in Figure 6, under the same driving time, the worse the road surface, the more likely it was to cause motion sickness. Different driving speeds had little effect on human motion sickness.

3.3.3. Impact of travel time

It could be known from the calculation results in Chapter 3.3.2 that the driving speed had no apparent influence on human motion sickness at the same driving time. When the speed was 80 km/h, the effect of

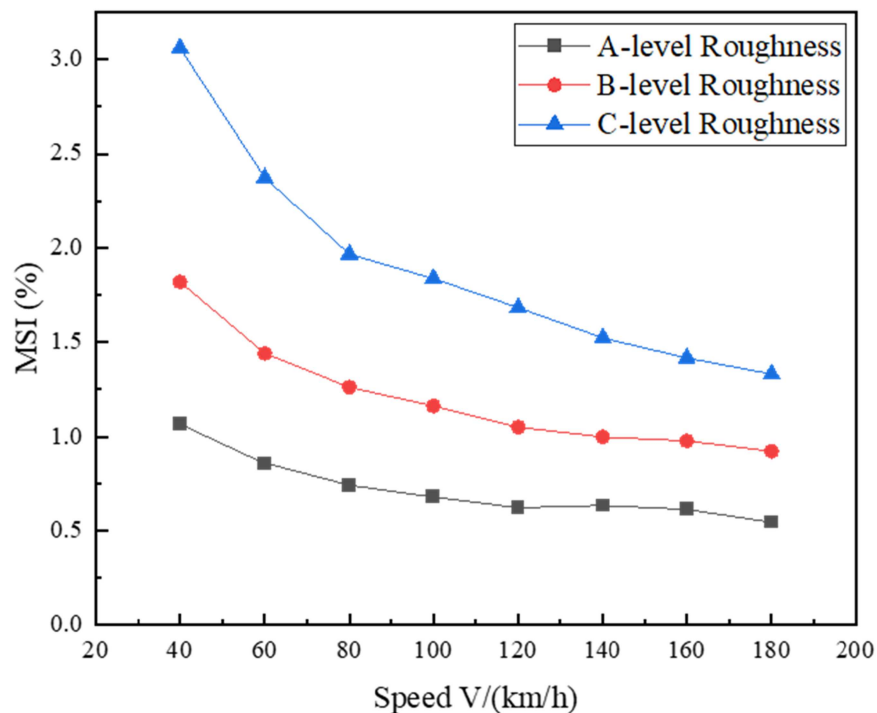


Figure 5. Motion sickness evaluation.

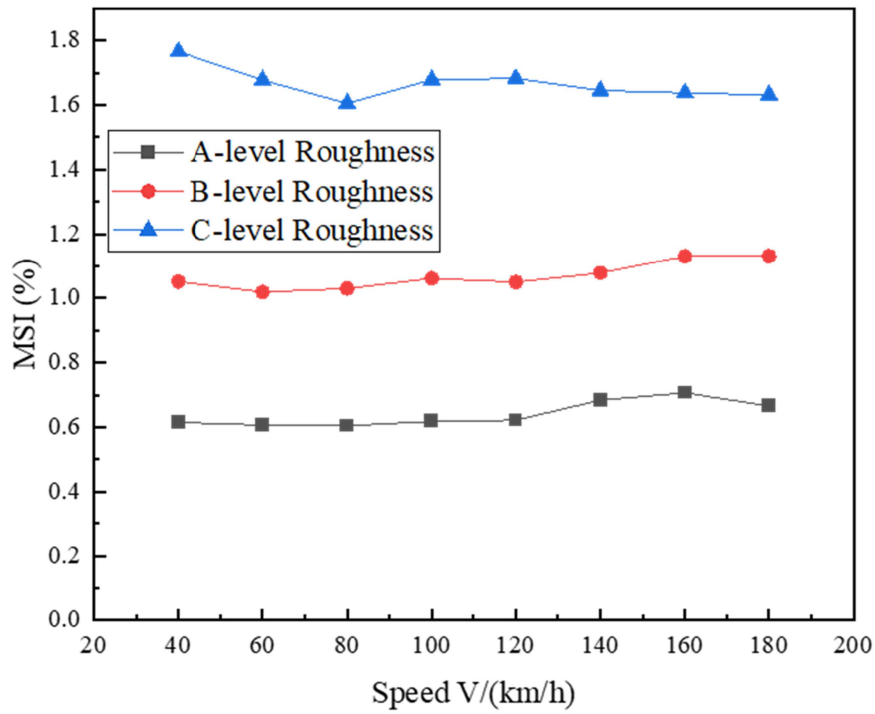


Figure 6. Motion sickness evaluation.

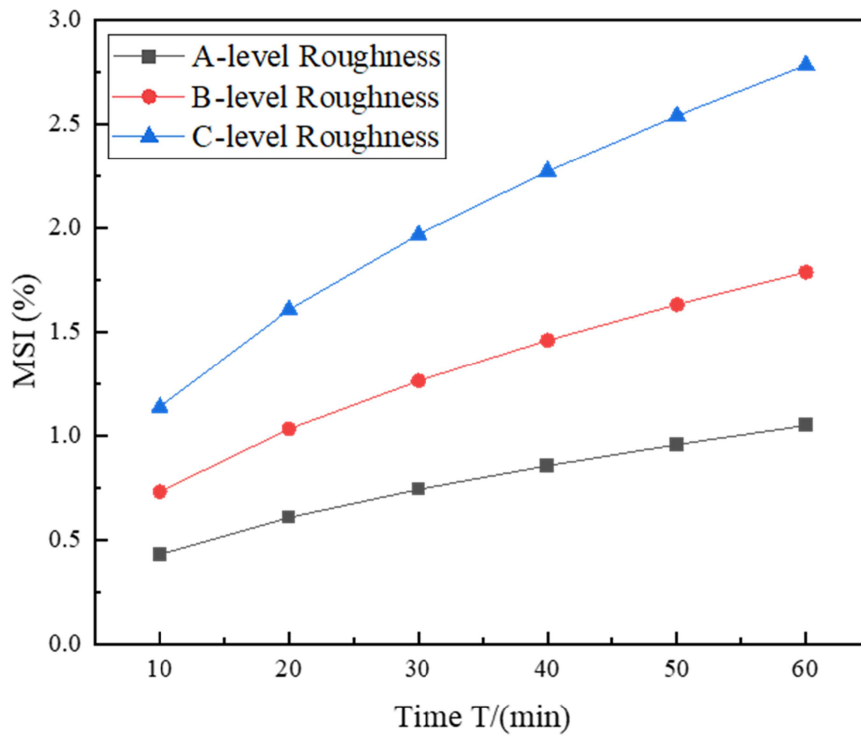


Figure 7. Motion sickness evaluation.

the car driving for different times under different pavement roughness excitation on driver motion sickness is shown in Figure 7.

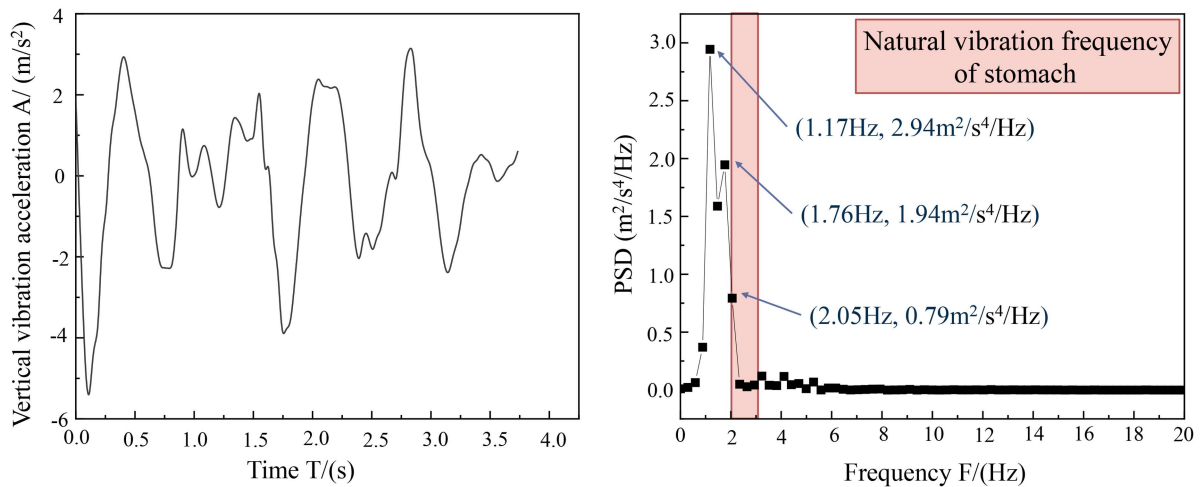
It could be seen from Figure 7 that the MSI had a linear relationship with the driving time at a certain driving speed. Meanwhile, the results of polynomial curve fitting are shown in Table 4.

Table 4. Function fitting of MSI with time.

Pavement roughness	Function expression (math.)	R^2
A-level	$MSI = 0.01218t + 0.3452$	0.9846
B-level	$MSI = 0.02078t + 0.5884$	0.9849
C-level	$MSI = 0.03237t + 0.9164$	0.9848

Table 5. Motion sickness time selection limits for vehicle driving.

Pavement roughness	MSI (%)			
	1	10	20	30
A-level	54 min	13 h	27 h	40 h
B-level	20 min	7 h	15 h	23 h
C-level	3 min	5 h	10 h	15 h

**Figure 8.** Time-domain and PSD curves of vertical vibrations of the stomach.

From Figure 7 and Table 4, it could be seen that the linear relationship between the driving time and the motion sickness indicator was good and the worse the pavement roughness, the greater the slope of the straight line. When the pavement level deteriorated from A to C, the slope of the straight line increased by 156.76%. The cumulative driving time statistics of the passenger car on different road roughnesses correspond to different motion sickness levels, as shown in Table 5.

As shown in Table 5, there would be 1% of the passengers feeling dizzy and nauseous when the vehicle was driven for 54 min on a level-A rough pavement. The threshold of MSI would be reached when the cumulative driving time reached 40 h. The driver would start to get sick after 20 min when the vehicle was driven on the B-level uneven road. The upper limit of the MSI was reached when the driver's cumulative travel time reached 23 h. It could make 1% of the occupants uncomfortable in 3 min when the vehicle was driving on a C-class road surface and the cumulative driving time reached 15 h to reach the threshold of the human MSI.

The partial correlation analysis showed that the partial correlation coefficient between motion sickness and pavement roughness was 0.932 and the partial correlation coefficient between motion sickness and driving time was 0.8833. The relationship between motion sickness and road roughness was more pronounced. Therefore, the road surface roughness should be controlled and the reasonable driving time should be determined according to the road surface unevenness.

3.4. Analysis of vibration exposure risk to driver organs

Based on the time-domain curves of the vibration response of different parts of the human body, the PSD was calculated. Taking the stomach as an example, the vibration acceleration time-domain response and

PSD of the passenger car running at a speed of 120 km/h on the C-level rough surface are shown in Figure 8.

From Figure 8, it could be seen that the vertical vibration acceleration of the stomach fluctuated between $-6\sim 4$ m/s² when the car was travelling at 120 km/h on a Class C pavement. From the PSD curve, it could be seen that the vibration of the stomach was a low-frequency vibration with a frequency between 1~6 Hz. The dominant vibration frequencies of 1.17 Hz and 1.76 Hz were not included in the natural vibration frequency range of the stomach. The dominant frequency within the intrinsic vibration frequency range was 2.05 Hz and the corresponding power spectrum density was 0.79 m²/s⁴/Hz.

The results of the vibration PSD for each human organ under the influence of different pavement roughnesses and different speeds are shown in Figures 9–12.

As could be seen from Figures 9–12, the PSD of different parts of the human body changed in the corresponding natural frequency range with the increase in speed and deterioration of pavement roughness. Some curves overlapped because of the similar vibration responses of certain organs under the investigated conditions. The upper arm, heart and lungs, torso, kidneys and pelvis did not change significantly, while the head, stomach, liver and lumbar spine changed greatly, especially the largest impact on the stomach, followed by the lumbar spine. For different pavement roughnesses, the PSD values would increase significantly when the speed exceeded 100 km/h.

In order to analyse the impact of pavement roughness and driving speed on various organs of the human body, a partial correlation analysis was also conducted, as shown in Table 6.

It could be seen from Table 6 that the stomach, liver and lumbar spine were more affected by speed. This is because organs such as the stomach, liver and lumbar spine exhibit greater sensitivity to vehicle speed due to their location and mass distribution, which are more directly influenced by changes in inertial forces and excitation frequency with speed. In contrast, the vibration responses of other organs are more strongly governed by pavement roughness, as roughness primarily determines the amplitude of road-induced excitation transmitted through the vehicle structure.

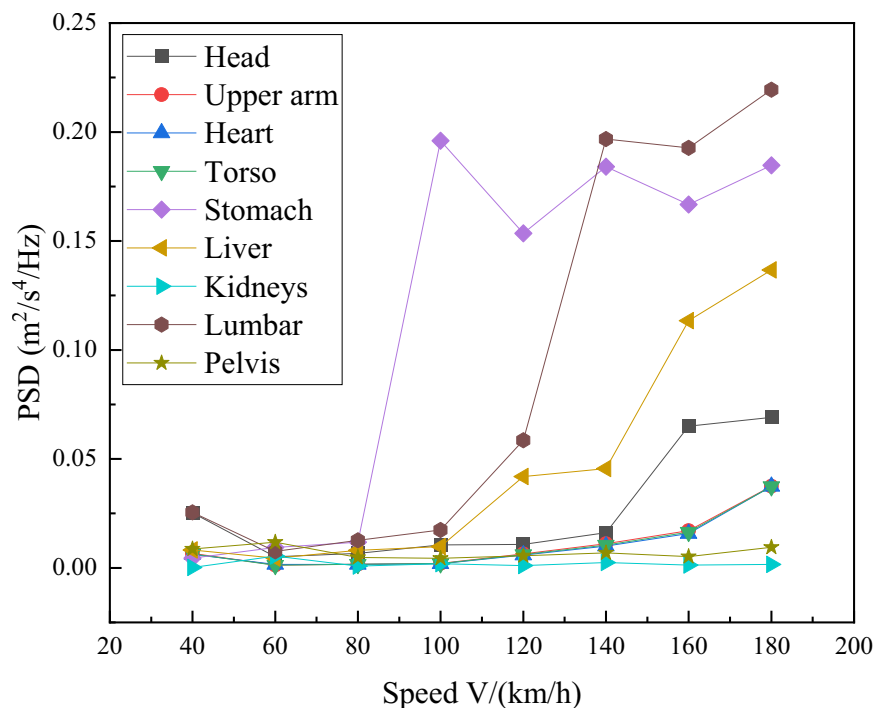


Figure 9. Acceleration PSD analysis for A-level pavement roughness.

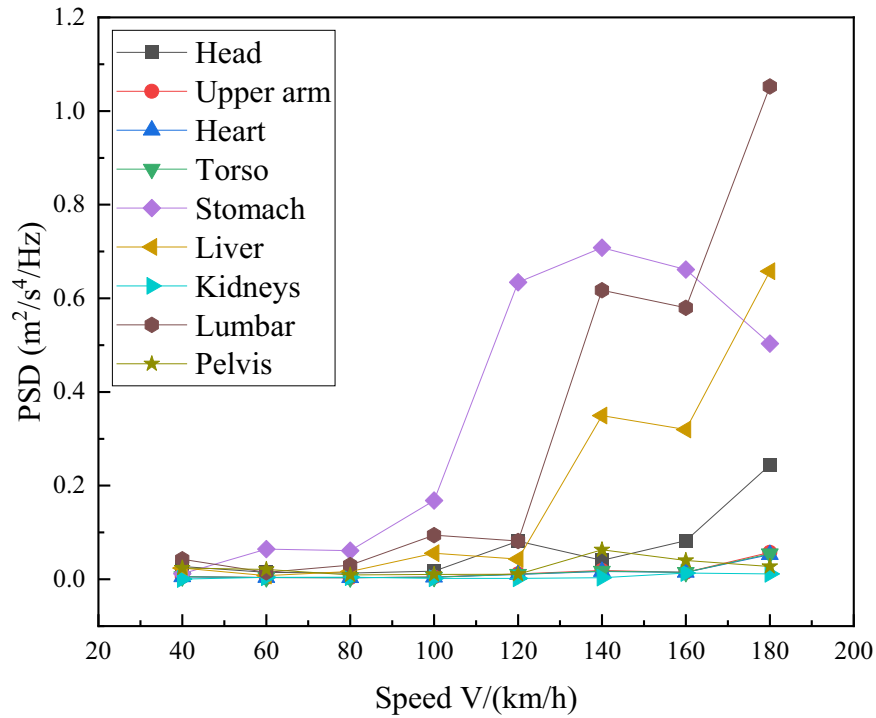


Figure 10. Acceleration PSD analysis for B-level pavement roughness.

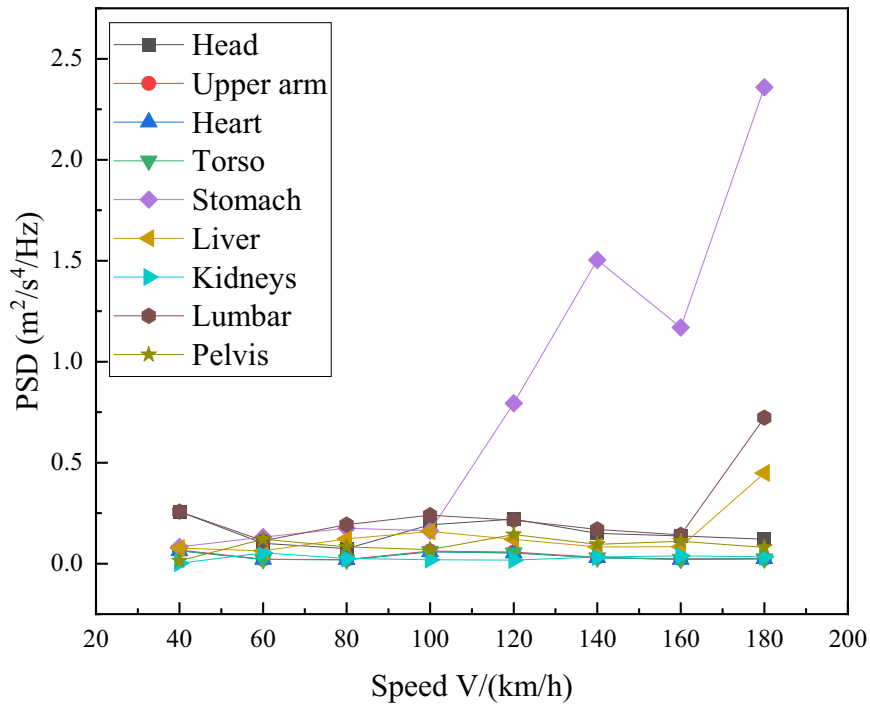


Figure 11. Acceleration PSD analysis for C-level pavement roughness.

4. Conclusion

In this paper, a 3D driver-vehicle coupled vibration model that can simultaneously calculate the vibration responses of various parts of both the vehicle and the driver was established. Based on the innovative

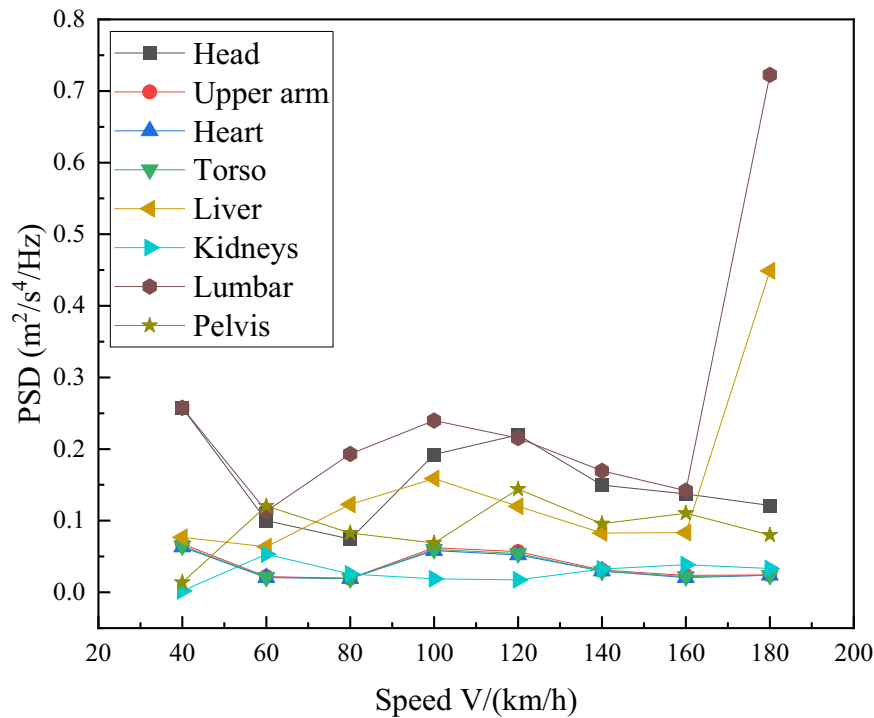


Figure 12. Acceleration PSD analysis for C-level pavement roughness without stomach.

Table 6. Partial correlation coefficient statistics.

Human organs	Partial correlation coefficient with pavement roughness	Partial correlation coefficient with driving speed
Head	0.7202	0.3452
Upper arm	0.6242	0.3004
Heart	0.6237	0.3033
Torso	0.6226	0.3021
Stomach	0.6312	0.7004
Liver	0.1989	0.645
Kidney	0.8045	0.288
Lumbar spine	0.2104	0.6373
Pelvis	0.8452	0.3049

model, driving comfort, motion sickness and vibration exposure risk to different organs were analysed. Partial correlation analysis was also used to explore the degree of influence of pavement roughness, driving speed and travelling time on the human body. The research results lay a theoretical foundation for the promotion of comfortable driving.

- (1) Driving comfort was directly related to pavement roughness and driving speed. Pavement roughness had the greatest influence on comfort, followed by driving speed. A reasonable driving speed should be determined according to the pavement roughness.
- (2) The MSI was most significantly affected by the pavement roughness. Its relationship with the driving speed depends on the evaluation condition. When the travel distance was fixed, higher speeds reduced the exposure time and thus resulted in a lower MSI. When the travel time was fixed, the MSI showed little variation with speed due to the constant exposure duration. Therefore, under specific operating conditions (e.g. driving on uneven roads), it is important to optimise the ride time according to the pavement roughness.
- (3) Vibration had a great significant impact on the head, stomach, liver and lumbar spine, especially on the stomach. In addition to the stomach, liver and lumbar spine, the vibration of the other organs was mainly affected by pavement roughness.

- (4) Within the scope of this study, maintaining pavement roughness at the PSD-based A level was beneficial for improving driving comfort and reducing motion sickness and vibration exposure risks. In addition, a critical speed range over 100 km/h was observed, at which the vibration responses of certain human organs exhibited noticeable amplification.

In summary, the proposed model and corresponding results provide theoretical guidance for improving driving comfort and reducing motion sickness and organ vibration exposure risk under steady-state driving conditions. The conclusions of this study are obtained assuming random pavement roughness excitation and uniform vehicle speed. In real traffic environments, additional dynamic effects caused by speed variations, braking and acceleration may further influence human vibration responses and motion sickness, which will be considered in future studies.

Moreover, although PSD-based pavement roughness is suitable for dynamic vibration analysis, establishing a quantitative relationship between PSD-based roughness characteristics and commonly used engineering indices, such as IRI, as well as identifying roughness spectral features that are most critical to motion sickness, remains an important direction for future research to enhance the practical applicability of the proposed framework.

Acknowledgements

This study is supported by the German Research Foundation (LI 3613/5-2, Project ID 414936990). The authors gratefully acknowledge the financial support.

Author contributions

None.

Disclosure statement

No potential conflict of interest was reported by the author(s).

ORCID

Pengfei Liu  0000-0001-5983-7305

Data availability statement

All data and models generated or used during the study appear in the published article.

References

- Asua, E., Gutiérrez-Zaballa, J., Mata-Carballeira, O., Ruiz, J. A., & Del Campo, I. (2022). Analysis of the motion sickness and the lack of comfort in car passengers. *Applied Sciences*, 12(8), 3717. <https://doi.org/10.3390/app12083717>
- Chang, C.-H., Stoffregen, T. A., Cheng, K. B., Lei, M. K., & Li, C.-C. (2020). Effects of physical driving experience on body movement and motion sickness among passengers in a virtual vehicle. *Experimental Brain Research*, 239(2), 491–500. <https://doi.org/10.1007/s00221-020-05940-6>
- Desai, R., Guha, A., & Seshu, P. (2021). Modelling and simulation of an integrated human-vehicle system with non-linear cushion contact force. *Simulation Modelling Practice and Theory*, 106, 102206.
- Fan, R., Liu, J., & Liu, J. (2021). Prediction of the natural frequencies of different degrees of degenerated human lumbar segments l2-l3 using dynamic finite element analysis. *Computer Methods and Programs in Biomedicine*, 209, 106352.
- Fan, R., Liu, J., Liu, J., & Wang, W. (2019). Presentation of an approach on determination of the natural frequency of human lumbar spine using dynamic finite element analysis. *Applied Bionics and Biomechanics*, 2019(1), 5473891.
- Fan, R. X., Liu, J., Li, Y. L., Liu, J., & Gao, J. Z. (2018). Finite Element Investigation of the Effects of the Low-Frequency Vibration Generated by Vehicle Driving on the Human Lumbar Mechanical Properties. *BioMed Research International*, 2018, 7962414. <https://doi.org/10.1155/2018/7962414>

- Hassan, R., & McManus, K. (2002). Perception of low frequency vibrations by heavy vehicle drivers. *Journal of Low Frequency Noise, Vibration and Active Control*, 21(2), 65–75. <https://doi.org/10.1260/026309202761019516>
- ISO. (1997). *Mechanical vibration and shock—Evaluation of human exposure to whole-body vibration. Part 1: General requirements* (ISO 2631-1) (Vol. N/A). ISO.
- Ji, Y., & Xing, Y. (2020). A two-sub-step generalized central difference method for general dynamics. *International Journal of Structural Stability and Dynamics*, 20(07), 2050071. <https://doi.org/10.1142/S0219455420500716>
- Li, J., Reda, A., & Butz, A. (2021). Queasy rider: How head movements influence motion sickness in passenger use of head-mounted displays. In C. P. Janssen, R. Schroeter, & P. Wintersberger (Eds.), *13th International Conference on Automotive User Interfaces and Interactive Vehicular Applications* (Vol. 2021, pp. 28–38). United Kingdom: Association for Computing Machinery. <https://doi.org/10.1145/3409118.3475137>
- Li, Y., & Wang, L. (2020). Computer-Aided Procedure for Analysis of Effect of Gradation and Compaction Temperature in Asphalt Mix Design by Using DEM. *Journal of Transportation Engineering, Part B: Pavements*, 146(239), 04020010. <https://doi.org/10.1061/JPEODX.0000159>
- Luo, S. (2021). Human Vehicle Dynamics Coupling of Miniature Electric Vehicle Roll Stability: Effects of Driver Weight, Wheel Base and Track Width Abstract. *Journal of Physics: Conference Series*, 2002(1), 012018. <https://doi.org/10.1088/1742-6596/2002/1/012018>
- Qassem, W, Othman, MO, & Abdul-Majeed, S (1994). The effects of vertical and horizontal vibrations on the human body. *Medical Engineering & Physics*, 16(2), 151–161.
- Song, B.-G., Bae, J.-J., & Kang, N. (2023). Uncertainty quantification of ride comfort based on GPC framework for a fully coupled human–vehicle model. *Applied Sciences*, 13(11), 6785.
- Taskin, Y., Hacioglu, Y., Ortes, F., Karabulut, D., & Arslan, Y. Z. (2018). Experimental investigation of biodynamic human body models subjected to whole-body vibration during a vehicle ride. *International Journal of Occupational Safety and Ergonomics*, 25(4), 530–544. <https://doi.org/10.1080/10803548.2017.1418487>
- Voicu, D., Stoica, R. M., Vilău, R., Marinescu, M., Digulescu, A., Despina-Stoian, C., & Popescu, F. (2023). Frequency analysis of vibrations in terms of human exposure while driving military armoured personnel carriers and logistic transportation vehicles. *Electronics*, 12(14), 3152. <https://doi.org/10.3390/electronics12143152>
- Wada, T., Sato, E., Orita, Y., Kida, S., Horita, H., & Rakumatsu, T. (2024). Effects of passenger body movements in a visual task during and after vehicle rotation on post-rotatory illusion and motion sickness. *Experimental Brain Research*, 242(6), 1455–1467. <https://doi.org/10.1007/s00221-024-06837-4>
- Wang, C., Wang, D., Liu, P., He, Y., & Oeser, M. (2023). Study on vehicle vibration response under the condition of 3D tire–pavement contact for unmanned driving. *Journal of Transportation Engineering, Part B: Pavements*, 149(1), 04022059.
- Wang, F., & Zhang, J. (2014). Riding comfort evaluation for asphalt pavement of highways. *Journal of Beijing University of Technology*, 40(3), 378–383.
- Wei, H., Wu, Y., Chen, X., & Xu, J. (2020a). A steering-following dynamic model with driver's NMS characteristic for human-vehicle shared control. *Applied Sciences*, 10(7), 2626. <https://doi.org/10.3390/app10072626>
- Wei, H., Wu, Y., Chen, X., Xu, J., & Rahul, S. (2020b). Human-vehicle dynamic model with driver's neuromuscular characteristic for shared control of autonomous vehicle. *Proceedings of the Institution of Mechanical Engineers, Part D: Journal of Automobile Engineering*, 237(10–11), 2402–2414.
- Więckowski, D. (2012). An attempt to estimate natural frequencies of parts of the child's body. *Archiwum Motoryzacji*, (1), 61–74.
- Wu, H., Wei, H., Liu, Z., & Xu, J. (2021). A simplified dynamic model with driver's NMS characteristic for human-vehicle shared control of autonomous vehicle. *Proceedings of the Institution of Mechanical Engineers, Part D: Journal of Automobile Engineering*, 236(1), 16–28.
- Zhang, J., Wang, M., Wang, D., Li, X., Song, B., & Liu, P. (2018). Feasibility study on measurement of a physiological index value with an electrocardiogram tester to evaluate the pavement evenness and driving comfort. *Measurement*, 117, 1–7. <https://doi.org/10.1016/j.measurement.2017.11.060>
- Zhu, J., Li, H., Xiong, Z., & Li, Y. (2023). Evaluation of whole body vibration of vehicle drivers on long-span highway suspension bridge experiencing vortex-induced vibration. *China Civil Engineering Journal*, 56(8), 60–84.